Second Harmonic Generation within a Random Fiber Laser

YOUSI YANG,[1,2] DAN LI,[1,2] PEI LI,[1,2] GUOHAO FU,[1,2] TIANCHENG QI,[1,2] YIJIE ZHANG,[1,2] PING YAN,[1,2] MALI GONG,[1,2] AND QIRONG XIAO[1,2*]

[1] *Department of Precision Instrument, Tsinghua University, No.1 Qinghua Garden, Chengfu Road, Haidian District, Beijing, P.R.China, 100084*
[2] *State Key Laboratory of Precision Space-time Information Sensing Technology, No.1 Qinghua Garden, Chengfu Road, Haidian District, Beijing, P.R.China, 100084*
*xiaoqirong@mail.tsinghua.edu.cn

Abstract: Optical fibers offer convenient access to a variety of nonlinear phenomena. However, due to their inversion symmetry, second-order nonlinear effects, such as second-harmonic generation (SHG), are challenging to achieve. Here, all-fiber in-core SHG with high beam quality is achieved in a random fiber laser (RFL). The fundamental wave (FW) is generated in the same RFL. The phase-matching-condition is mainly achieved through a periodically electric field induced and the gain is enhanced through the passive spatiotemporal gain modulation and the extended fiber. The conversion needs no pretreatment and the average second-harmonic (SH) power reaches up to 10.06 mW, with a corresponding conversion efficiency greater than 0.04%. Moreover, theoretical model is constructed to explain the mechanism and simulate the evolution of SH and FW. Our work offers a simple method to generate higher brightness in-fiber SH, and may further provide new directions for research on all-fiber $\chi^{(2)}$-based nonlinear fiber optics and RFLs.

Keywords: Second harmonic generation, Random fiber laser, Distributed feedback

1. Introduction

Owing to the small core diameter and excellent flexibility, optical fibers have found extensive applications in communication[1], sensing[2], medical diagnostics[3,4], and imaging[5,6]. Additionally, they are one of the most studied nonlinear media [7–12]. Numerous interesting research have been found, including supercontinuum generation[13–15], optical rogue waves[16,17], and third harmonic generation[18–20], and soliton generation[21]. However, second-order nonlinear processes theoretically cannot occur on account of the inversion symmetry of optical fibers. The development of related applications such as fiber-based harmonic sources, self-referencing of frequency combs, parametric down-conversion sources and fiber-based quantum communication is therefore limited. Second harmonic generation (SHG), as a typical second-order nonlinear process[22], can serve as an intuitive measure for estimating the value of second-order susceptibility ($\chi^{(2)}$). By implementing SHG within optical fibers, it can provide stable and simple solutions for various fields, for example, biomedical, visible-light communication, underwater communication, optical storage, and so on.

10.1017/hpl.2025.25

There have been many studies using fiber sources to excite SHG in other media[23,24]. Within fibers, SHG was observed in the last century [25–29], and studies have explored phase-matching conditions in both the fiber core and cladding[26,29–31]. For commonly used commercial or telecom fibers, Cherenkov-type radiation phase-matching can be more easily satisfied in the cladding[30], while phase-matching in the core can be attributed to the excitation of periodically electric fields[32–35]. These fields rearrange charges, forming a periodic array of dipoles, with the periodicity matching the requirements for phase-matching. The entities involved in dipole formation could be defects, color centers, or traps. At that time, the output SH powers were relatively low and required high-peak-power pulsed excitation sources [8,25,36]. To enhance the output power, quasi-phase-matching techniques were implemented in fibers, often combined with poling techniques such as thermal poling [37]. Employing these methods, milliwatt-level SH power was readily achieved, and conversion efficiency was improved [38,39]. However, poling techniques demand complex preprocessing. Their intricate processes limit the achievable fiber lengths, and the conversion bandwidth is narrow, typically around 0.5 nm for 30 cm long poled fiber samples [40]. More recently, studies have focused on integrating materials with substantial second-order nonlinearity into optical fibers [41–43]. But the output power remains low, typically in the nanowatt range or lower [44–46]. Moreover, in the aforementioned methods, the fundamental wave source (FW) and SH generator are often discrete, reducing integration. Overall, in-core SHG still faces one or more challenges such as low average power, complex preprocessing, or the separation of FW source and the SHG medium.

Recently, there have been many interesting studies. In RFLs, scattered second and third harmonics propagating in the cladding have been observed in single mode fibers and verified to meet the Cherenkov radiation phase-matching conditions [47,48]. Although the harmonics were not in-core[48], a high-integration solution that requires no preprocessing was provided. There are other studies that have found visible light in fibers[49–52]. The guided modes of visible light originated from inter-mode four-wave mixing [51] and cascaded four-wave mixing[52]. In addition, the effective shortwave extension of the spectrum driven by the geometrical parameter instability effect in the graded-index multimode fiber has been deeply investigated[53–57]. However, in-core SHG has not been observed in these researches. This is because the phase matching conditions are difficult to satisfy, the SHG gain in the core is weak, and there is competition from other nonlinear effects. Although extending the fiber length can enhance the SHG gain, it also leads to stronger scattering losses.

In this work, we utilize an RFL to generate SH in a single-mode fiber without external FW. The SH can be directly output from the fiber core. Phase-matching condition in the core is automatically satisfied due to the periodic electric field induced. No preprocessing techniques such as thermal poling or material integration are required. Distributed feedback and strong point feedback form a random cavity, while SHG process provides gain. The gain is enhanced due to the passive spatiotemporal gain modulation and the extended fiber. The output power of the SH band reaches a maximum of 10.06 mW, with a corresponding conversion efficiency from the FW to the SH greater than 0.04%. The temporal characteristics of the SH band are measured, revealing the occurrence of optical rogue waves. We establish a theoretical model for SHG in RFL to qualitatively explain the operation principle, and further combine it with the generalized nonlinear Schrödinger equations (GNLSEs). A more accurate spatial evolution of the spectrum can be simulated. In summary, we identify an RFL structure that can simultaneously generate both the FW and SH. The proposed structure is capable of directly emitting milliwatt-level SH from the fiber core. A simple method for generating in-core SH at a low threshold is demonstrated, involving complex dynamical processes within the random fiber cavity. The results may spark further research in all-fiber $\chi^{(2)}$-based nonlinear fiber optics and RFLs.

2. Experiments and results

https://doi.org/10.1017/hpl.2025.25 Published online by Cambridge University Press

2.1. Design of the RFL configuration

The experimental structure of the RFL is shown in Fig. 1(a). The output light of two 976 nm LDs is coupled into the inner cladding of a 10/130 μm fiber via a (2+1)×1 beam combiner and injected into a 7 m-long YDF, where the pump 976 nm light is converted into 1070 nm FW. Subsequently, the unabsorbed pump light in the cladding is filtered out using a CPS. The core light is injected into a 1 km-long communication fiber (G652D). The output end of G652D is angle-cleaved to avoid Fresnel reflection. In the backward output direction, the signal arm of the combiner is connected to a 1070 nm HR FBG, forming a half-open cavity ytterbium RFL. The other end of the grating is connected to a single arm of a 2×1 coupler. The other two arms of the coupler are fused together directly, making the coupler a Sagnac fiber loop mirror (FLM)[58–61].

Fig. 1(b) illustrates the feedback mechanism in our structure. Rayleigh scattering results in the conversion of a portion of the FW and SH propagating within the fiber into scattered light in multiple directions. A fraction of the scattered light that meets the conditions for total internal reflection is confined within the fiber core. This backscattered light allows the FW to undergo ytterbium ion gain or Raman gain. The backscattered SH can also be amplified. The purpose of employing FLM is to introduce strong broadband feedback, enabling the reverse propagation of backscattered light for further amplification through both YDF and GDF. This setup forms a random cavity via point feedback and distributed feedback, providing feedback for both the FW and SH. Details regarding how the phase-matching conditions are satisfied in the fiber core, as well as other relevant mechanisms, will be discussed in the **Discussion** section. Notably, the FW is generated in the form of pulses. This intentional design stems from the fact that passive spatiotemporal gain modulation within RFLs induces pulsed laser operation[62]. The pulsed FW can significantly augment their peak power and SH conversion efficiency. In addition, the higher power at 1070 nm effectively triggers stronger nonlinear effects, thereby increasing spectral components and facilitating SH generation from the FW. Consequently, broadband SH can be generated without necessitating multiple FW sources. In contrast to injecting FW laser output into an SH generator, here both FW and SH are generated within the same scheme, offering superior integration. Also, the continuous operation mode of LD enhances the pump injection capability, enabling higher average power SHG.

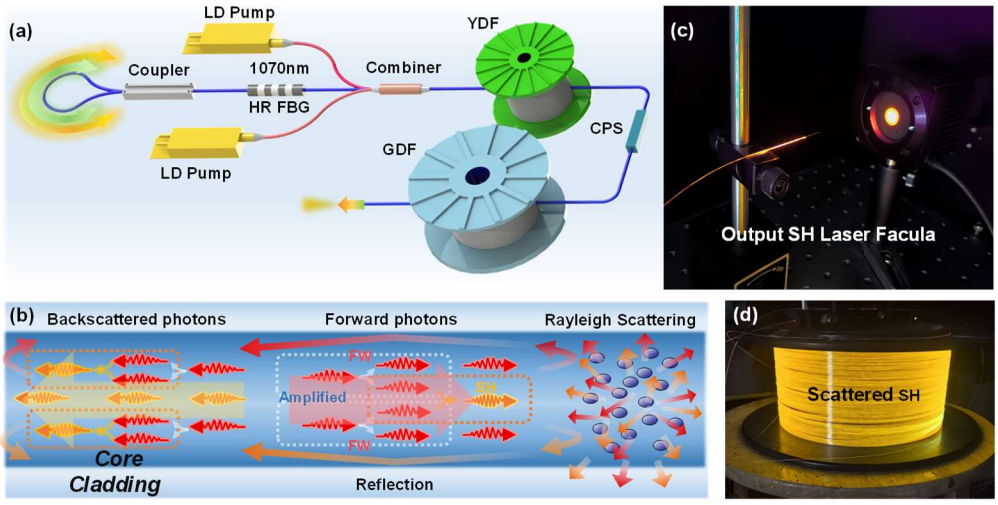

Fig. 1. (a) Experimental setup. LD Pump: laser diode pump. HR FBG: high-reflectivity fiber Bragg grating. YDF: ytterbium-doped fiber. GDF: Germanium-doped fiber. CPS: cladding power stripper. (b) Principle of SH gain and feedback. (c) Output SH laser facula after a

https://doi.org/10.1017/hpl.2025.25 Published online by Cambridge University Press

cladding light stripper attached to the output (d) GDF glowing visible light while the pump is injected.

2.2. Evolution of output spectrum and SH signal power

During the experiment, accompanied by pump injection, a circular visible light spot can be immediately observed at the output end (Fig. 1(c)). This indicates that SH can be generated, transmitted and output within the fiber core. Additionally, scattered visible light from the fiber cladding is also observed (Fig. 1(d)). These lights are the SHs in the cladding, for which the phase matching condition is directly satisfied, i.e., the Cherenkov-phase-matched harmonic conversion[48]. Our primary focus is on the SH output directly from the fiber core. To obtain this light spot, a cladding light stripper is connected to the output fiber. The spectrum and power are directly measured at the output end. The measured output spectra at different pump powers are shown in Fig. 2. For the structure of RFL, there exists a sequential relationship. The ytterbium RFL formed by the HR FBG takes precedence, which is in an internal position. Externally, there is the broadband RFL provided feedback by the FLM. The ytterbium-gain RFL, composed of a 1070 nm HR FBG, ensures the gain priority of 1070 nm light in the YDF, which can enhance the robustness of the system. Additionally, the higher optical power at 1070 nm effectively excites nonlinear effects within the GDF, giving rise to increased spectral components and promoting SHG from the FW. Initially, when LD pump power is injected, the ytterbium-gain RFL starts operation, leading to the appearance of a peak at 1070 nm in the output spectrum (Fig. 2(a)). At this stage, because the pump power is close to the laser threshold, there are many random noise peaks in the spectrum. They are attributed to the interaction between Rayleigh scattering and stimulated Brillouin scattering effects, which leads to the occurrence of self-Q-switching[63–66]. The self-Q-switching effect also induces strong pulses in the temporal domain, thereby stimulating the SHG process. The feedback provided by the FLM and Rayleigh scattering forms a random cavity for SH, hence, besides the noise peaks, there is also a visible peak at 535 nm.

When the LD pump power exceeds the laser threshold and reaches the threshold for cascaded SRS effects (Fig. 2(b)), random noise peaks are no longer present. With the pedestal elevating, the spectrum transitions to a supercontinuum. In the near-infrared wavelength range, there are five peaks observed: the 1070 nm and its first, second, and third-order Stokes lights, as well as a minor peak at 976 nm representing the unabsorbed LD light. The spectrum spans from 680 nm to 2116 nm. The extension towards shorter wavelengths is attributed to the participation of cascaded SRS Stokes light in cascaded four-wave mixing (FWM) effects[49,52]. Despite the broadening of the spectrum, the intensities of the 1070 nm laser and its cascaded Raman Stokes light exceed the pedestal by tens of dB. These high intensity light serve as multi-wavelength FWs for the SHG process and bring about an increase in spectral components in the SH band. The peak at 592 nm becomes predominant rather than 535 nm. This phenomenon can be explained as follows: compared to the 535 nm green light, the 592 nm orange light experiences lower losses in the fiber. Additionally, a considerable amount of 1070 nm laser is converted to Raman Stokes light, and the power of the 1184 nm Raman light is sufficient to stimulate SHG. These two conditions lead the 592 nm orange light to dominate the competition.

Fig. 2(c) indicates that after the transition to a supercontinuum, further increasing the pump power does not significantly broaden the spectral range. Instead, it promotes energy transfer to higher-order Stokes light and further enhances SHG. In the SH band, the peaks at 535 nm, 561 nm, 592 nm and 621 nm originate from the 1070 nm light, the first-order SRS Stokes light, the second-order SRS Stokes light, and the third-order SRS Stokes light, respectively. The SH band spectrum covers from 520 nm to 650 nm, spanning 130 nm. Fig. 2(d) is the comparison of SH spectra, showing higher spectrum intensity and more spectral

https://doi.org/10.1017/hpl.2025.25 Published online by Cambridge University Press

components under 20.88 W FW power. It should be noted that, in our structure, the FW neither undergoes conversion to the third harmonic nor generates other visible light peaks due to cascaded four-wave mixing, phenomena which have been observed in previous studies[48,51]. The former is because the fiber used exhibits high loss for the third harmonic corresponding to the FW, placing it at a disadvantage in terms of gain competition. The latter is due to the inability of inter-modal four-wave mixing to occur in single-mode fibers. The spectrum of the SH band is not connected to the spectrum of the near-infrared band, which is different from the visible light spectrum induced by dispersion waves in other studies[53].

By adjusting the power of the pump LD, the evolution of total output power at different pump powers can be measured (see in Note.S1, Supplementary material). Furthermore, the SH power at different FW powers is obtained, as depicted in Fig. 2(e). The SH power is measured after isolating other optical frequencies using a dichroic mirror and multiple optical filters. The FW powers are determined through spectral integration. The calculation method is shown in Note.S2, Supplementary material. At our maximum pump power, the output SH power is 10.06 mW. Further increasing the pump power can generate higher SH power.

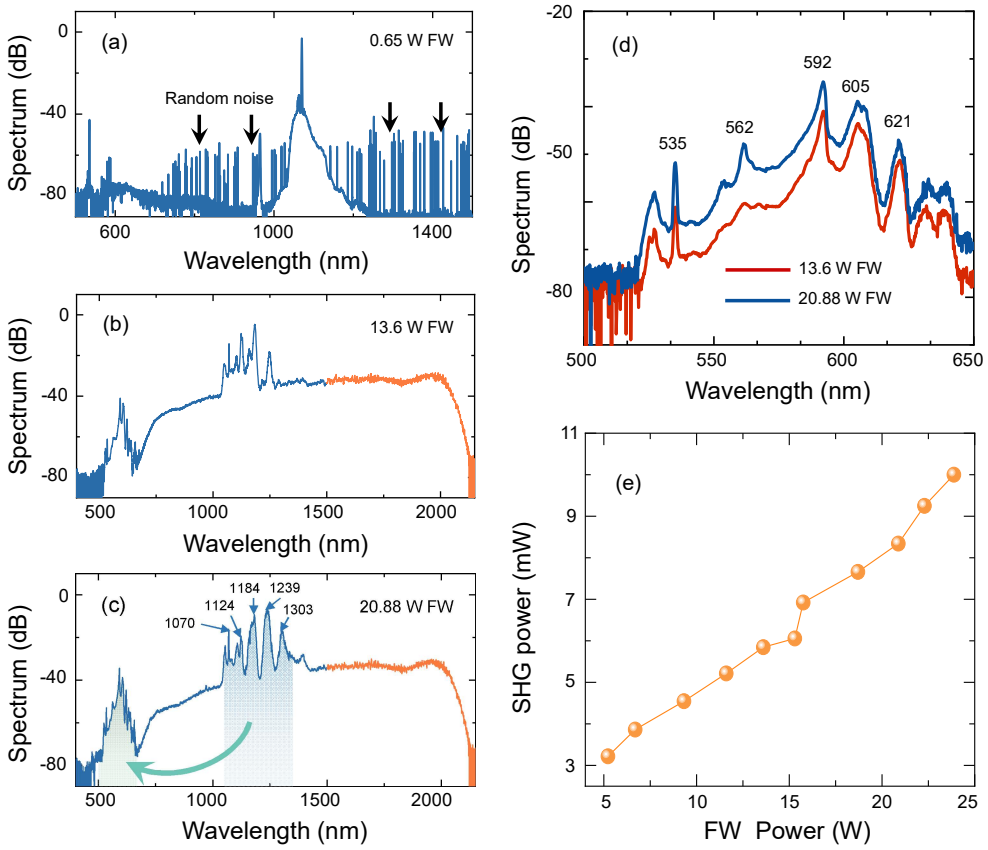

Fig. 2. Measured spectra with the FW powers of (a) 0.65 W, (b) 13.6 W and (c) 20.88 W. (d) Comparison of SH band spectra with the FW powers of 13.6 W and 20.88 W. (e) The SHG output power with the increase of the FW power.

2.3. Temporal characteristics of the SH band signal

After separating the light of the SH and FW bands using a dichroic mirror and filters, the waveforms of these two bands are measured separately. The pulse operation characteristic of the FW in this RFL provides the possibility for rapid generation of SH and causes pulsed

https://doi.org/10.1017/hpl.2025.25 Published online by Cambridge University Press

behavior of SH in the temporal domain. The temporal characteristics of the FW are measured, manifesting as pulses with widths of tens of nanoseconds. The pulses arise from passive spatiotemporal gain modulation of the pump light. The pulsed FW have a repetition rate, although it may fluctuate. As an example at maximum output power, the waveforms of the FW are measured. Due to the wide spectral range, both Si-based detector (Thorlabs, DET025A) and InGaAs-based detector (Thorlabs, DET08C) are utilized. According to the measurement results, the waveforms measured by the Si-based detector exhibit a 12 μs pulse repetition period (Fig. 3(a)), while those measured by the InGaAs-based detector exhibit a 10 μs period (Fig. 3(b)). It should be noted that the waveform period measured with InGaAs-based detector is unstable with very small fluctuations. The pulses of 1070 nm are rapidly consumed and then generated with a stable period. The energy of 1070 nm light will be converted to other wavelengths, mainly the Raman Stokes light. However, the further power consumption involves complex competition among nonlinear effects, which can interfere with the power consumption. More details are shown in Note.S3, Supplementary material.

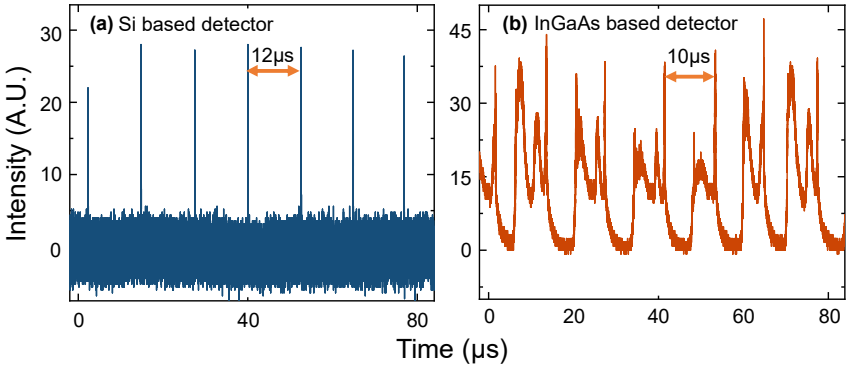

Fig. 3. Measured waveforms of the FW by (a) Si-based detector and (b) InGaAs-based detector.

Here, we mainly focus on the temporal characteristics of SH, which cannot be directly measured using Si-based detectors due to the presence of other dispersive waves above 680 nm. Optical filtering devices are used to reduce the stray light spectrum intensity to a negligible level. Fig. 4(a) displays the temporal waveforms of SH under different FW powers, exhibiting significant fluctuations in waveform intensity and the presence of pulses with intensities far exceeding others, suggesting the occurrence of optical rogue waves. The peak voltages of the pulses are extracted as events information and the histograms of the recorded events are plotted to obtain the statistical distribution, as shown in Fig. 4(b). The histograms clearly show the L-shaped distribution of optical rogue waves, with the gray area representing noise. The vertical dashed lines indicate the peak amplitude twice the significant wave height (SWH). SWH can be defined as the mean height of the highest third of events[67]. The appearance of optical rogue waves is unexpected because the intensity fluctuations of the FW are far from being such obvious. Moreover, the SH band is also in the normal dispersion region of the fiber, making modulation instabilities not easy to appear. We speculate that the possible reason is the dynamic change in the proportion of the FW participating in SHG process. The FW undergo various nonlinear effects such as SRS, FWM, and modulation instabilities simultaneously in the fiber, with dynamic competitive relationships among these effects. Since there is originally a small part of FW involved in SHG, at certain moments, more FW participate, such increase in proportion is sufficient to significantly enhance the SH waveform intensity. On the other hand, the distribution of signal power itself can also change the distribution of the $\chi^{(2)}$, which in turn influences the conversion efficiency, so the perturbation of intensity can be amplified. As the FW power increases, more waveforms with

https://doi.org/10.1017/hpl.2025.25 Published online by Cambridge University Press

intermediate intensities appear in the histogram, starting to evolve towards a flatter distribution. This implies that further improving the pump power may reduce the probability of rogue wave occurrence.

The individual waveform of the rogue waves is depicted in Fig. 4(c). It is worth noting that although the pulse widths of the rogue waves are on the order of nanoseconds, the actual widths are likely to be lower and accurate measurement is limited by the bandwidth of the detector. SHG for different FW wavelengths corresponds to $\chi^{(2)}$ with different periods. Therefore, SHs of different wavelengths are generated at different positions within the fiber, resulting in slight differences in the output timing. As can also be observed in Fig. 4(c), when the FW power increases, additional pulse peaks appear beside the main peak, which can be treated as the SH from other FW with lower intensity.

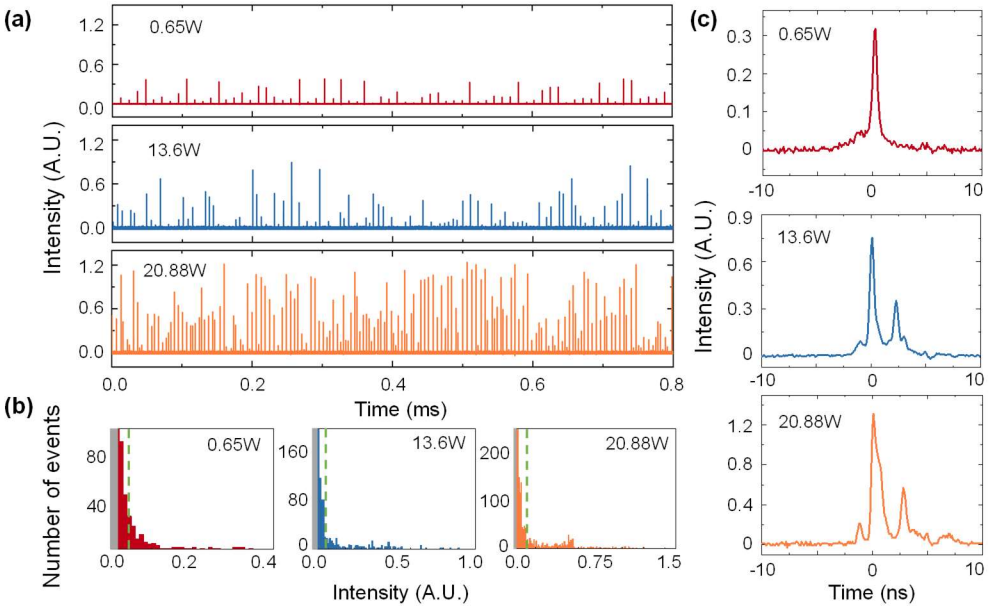

Fig. 4. Temporal characteristics of the SH band with different FW powers. a) Wide time range waveforms. b) Histogram of the pulse intensity distribution. c) Single waveform measurement result.

3. Discussion

Next, we perform a simulation analysis of our experimental results. In terms of the cladding SH, it has been already conducted in-depth studies[48]. Our focus is primarily on the in-core SH, as it exhibits better beam quality. There are two key reasons that this RFL can generate in-core SH efficiently rather than completely depleting it. Firstly, SH has received sufficient feedback. The point feedback and distributed feedback form a random cavity. The feedback band covers the SH band, allowing a portion of the scattered SH to return to the passive fiber for amplification. Secondly, due to the passive spatiotemporal modulation of the pump light in the half-open cavity structure, the FW propagates in the form of pulse light, with high peak power enhancing the SH gain. To verify the influence of these two factors, a theoretical model is established based on the self-organized SHG theory[68]. This theory links induced $\chi^{(2)}$ with the presence of germanium dopants which lead to the appearance of defects that trap electrons. The electrons are transferred from Ge-centers to a silica matrix or to a different Ge-center under pumping[33]. These electrons are referred to as charge transfer excitons

https://doi.org/10.1017/hpl.2025.25 Published online by Cambridge University Press

(CTE)[31].The delocalization of charges enhances $\chi^{(2)}$, and amplify the polarization P_{dc}^{0} and the corresponding field E_{dc}^{0}. The periodic electric field participates in and drives the SHG process. The excitation of the electric field is associated with FW injection and one photon absorption of SH[31]. In our structure, the initial SHG can arise from various mechanisms, including the surface nonlinearity of fiber core cladding interface, nonlinearity derived from electric quadrupole moment or magnetic dipole moment and SH in the cladding which is generated based on Cherenkov-type radiation phase-matching.

The amplitudes A_0, A_1, A_2 and phases ψ_0, ψ_1, ψ_2 of static, fundamental and SH fields are introduced, respectively, as variables. The corresponding physical fields are[68]:

$$\begin{aligned} &-A_0 e^{i(\psi_0 + k_2 z - 2ik_1 z)} + h.c., \\ &A_1 e^{i(\psi_1 + k_1 z - \omega t)} + h.c., \\ &A_2 e^{i(\psi_2 + k_2 z - 2\omega t)} + h.c.. \end{aligned} \tag{1}$$

It can be seen that the phase-matching condition is automatically satisfied through this electric field. For the electric field, its saturated form should be a solution of the following equation:

$$\frac{\partial(-A_0 e^{i\psi_0})}{\partial t} = -\alpha A_2^2(-A_0 e^{i\psi_0} + u e^{i\psi_2 - 2i\psi_1}). \tag{2}$$

For the fundamental and SH fields, the wave equations for slow variables are:

$$\begin{aligned} n_2 \frac{\partial(A_2 e^{i\psi_2})}{\partial z} &= i\frac{4\pi\omega}{c} P_{2\omega}, \\ n_1 \frac{\partial(A_1 e^{i\psi_1})}{\partial z} &= i\frac{2\pi\omega}{c} P_{\omega}, \end{aligned} \tag{3}$$

where $P_{2\omega}$ and P_{ω} are ordinary $\chi^{(3)}$ nonlinear terms,

$$\begin{aligned} P_{2\omega} &= -\chi_2^{(3)} A_0 A_1^2 (e^{i\psi_0 + 2i\psi_1}), \\ P_{\omega} &= -\chi_1^{(3)} A_0 A_1 A_2 (e^{-i\psi_0 - i\psi_1 + i\psi_2}). \end{aligned} \tag{4}$$

Thus,

$$\begin{aligned} n_2 \frac{\partial(A_2 e^{i\psi_2})}{\partial z} &= i\frac{4\pi\omega}{c}(-\chi_2^{(3)}) A_0 A_1^2 (e^{i\psi_0 + 2i\psi_1}), \\ n_1 \frac{\partial(A_1 e^{i\psi_1})}{\partial z} &= i\frac{2\pi\omega}{c}(-\chi_1^{(3)}) A_0 A_1 A_2 (e^{-i\psi_0 - i\psi_1 + i\psi_2}). \end{aligned} \tag{5}$$

The final equations for normalized variables:

$$\begin{aligned} &E_0 = \frac{A_0}{u}, \quad E_1 = \frac{A_1}{u}, \quad E_2 = \frac{A_2}{u}, \\ &S = \kappa_0 z, \quad \tau = \alpha_2 u^2 t, \\ &\widetilde{\alpha_i} = \frac{\alpha_i}{\kappa_0}, \quad \kappa_0 = \frac{4\pi\omega\chi^{(3)}u^2}{c}, \end{aligned} \tag{6}$$

following from Eqs. (S2) and (S4). There are[68]:

https://doi.org/10.1017/hpl.2025.25 Published online by Cambridge University Press

$$\begin{aligned}
\frac{\partial E_2}{\partial S} &= E_0 E_1^2 \sin(\psi_0 + 2\psi_1 - \psi_2), \\
E_2 \frac{\partial \psi_2}{\partial S} &= -E_0 E_1^2 \cos(\psi_0 + 2\psi_1 - \psi_2), \\
\frac{\partial E_1}{\partial S} &= -E_0 E_1 E_2 \sin(\psi_0 + 2\psi_1 - \psi_2), \\
E_1 \frac{\partial \psi_1}{\partial S} &= -E_0 E_1 E_2 \cos(\psi_0 + 2\psi_1 - \psi_2), \\
\frac{\partial E_0}{\partial \tau} &= -E_2^2 (E_0 - \cos(\psi_0 + 2\psi_1 - \psi_2)), \\
E_0 \frac{\partial \psi_0}{\partial \tau} &= -E_2^2 \sin(\psi_0 + 2\psi_1 - \psi_2).
\end{aligned} \tag{7}$$

In our modified model, the distributed feedback provided by Rayleigh scattering are introduced. Naturally, it is necessary to distinguish between forward and backward light in the fiber, both for the SH and the FW. To simplify the model, forward and backward SHs are assumed to originate solely from forward and backward FWs, respectively. Additionally, fiber losses for both SH and the FW are taken into account, as this involves losses within the cavity. The equations are as follows:

$$\frac{\partial E_2^{\pm}}{\partial S} = E_0 (E_1^{\pm})^2 \sin(\psi_0 + 2\psi_1^{\pm} - \psi_2^{\pm}) - \frac{\alpha_{2\omega}^n}{2} E_2^{\pm} + \frac{\varepsilon_{2\omega}^n}{2} E_2^{\mp}, \tag{8}$$

$$E_2^{\pm} \frac{\partial \psi_2}{\partial S} = -E_0 (E_1^{\pm})^2 \cos(\psi_0 + 2\psi_1^{\pm} - \psi_2^{\pm}),$$

$$\frac{\partial E_1^{\pm}}{\partial S} = -E_0 E_1^{\pm} E_2^{\pm} \sin(\psi_0 + 2\psi_1^{\pm} - \psi_2^{\pm}) - \frac{\alpha_{\omega}^n}{2} E_1^{\pm} + \frac{\varepsilon_{\omega}^n}{2} E_1^{\mp}, \tag{9}$$

$$E_1^{\pm} \frac{\partial \psi_1^{\pm}}{\partial S} = -E_0 E_1^{\pm} E_2^{\pm} \cos(\psi_0 + 2\psi_1^{\pm} - \psi_2^{\pm}),$$

$$\begin{aligned}
\frac{\partial E_0}{\partial \tau} &= -(E_2^{\pm})^2 (E_0 - \cos(\psi_0 + 2\psi_1^{\pm} - \psi_2^{\pm})), \\
E_0 \frac{\partial \psi_0}{\partial \tau} &= -(E_2^{\pm})^2 \sin(\psi_0 + 2\psi_1^{\pm} - \psi_2^{\pm}),
\end{aligned} \tag{10}$$

where $\alpha_{2\omega}^n$ and α_{ω}^n represent the normalized loss terms for the SH and FW, respectively, and $\varepsilon_{2\omega}^n$ and ε_{ω}^n denote the coefficients of Rayleigh scattering light of the SH and FW being total-reflected. The cavity is formed through distributed feedback and point feedback. Distributed feedback is manifested through the Rayleigh scattering term, while point feedback is reflected at the boundaries. More detailed explanations about this model can be found in Note S4, Supplementary material. Utilizing the modified self-organized SHG model, under the same pumping and initial conditions, the evolution of SH in both the fiber without FLM feedback and the half-open cavity RFL are analyzed. This part of the simulation is also shown in Note S4, Supplementary material.

However, for FW, it is inaccurate to consider only its loss and assume that FW is just directly injected into the fiber. This is because FW is generated from the same RFL, and its energy will spread to a wider frequency range. By incorporating FW gain and conversion to other wavelengths, a more precise evolution of the SH field within this RFL can be provided. A detailed theoretical model is based on the GNLSEs taking the dispersion effect, self-phase modulation, cross-phase modulation, cascaded Raman scattering, average Rayleigh scattering and SHG into account:

https://doi.org/10.1017/hpl.2025.25 Published online by Cambridge University Press

$$\pm\frac{\partial A_0^{\pm}}{\partial z}+\frac{1}{v_{g,0}}\frac{\partial A_0^{\pm}}{\partial t}+\frac{i\beta_{2,0}}{2}\frac{\partial^2 A_0^{\pm}}{\partial t^2}-\frac{\beta_{3,0}}{6}\frac{\partial^3 A_0^{\pm}}{\partial t^3}=i\gamma_0\left(\left|A_0^{\pm}\right|^2+2\sum\nolimits_{k\neq 0}\left|A_k^{\pm}\right|^2\right)A_0^{\pm}+i\frac{2\pi\omega}{c}P_{\omega,0}$$
$$-\frac{g_R(\Delta\omega)}{2}\left(\left|A_1^{\pm}\right|^2+\left|A_1^{\mp}\right|^2\right)A_0^{\pm}-\frac{\alpha}{2}A_0^{\pm}-\frac{\varepsilon(\omega)}{2}A_0^{\pm}+\frac{\varepsilon(\omega)}{2}A_0^{\mp}, \quad (11)$$

$$\pm\frac{\partial A_i^{\pm}}{\partial z}+\frac{1}{v_{g,i}}\frac{\partial A_i^{\pm}}{\partial t}+\frac{i\beta_{2,i}}{2}\frac{\partial^2 A_i^{\pm}}{\partial t^2}-\frac{\beta_{3,i}}{6}\frac{\partial^3 A_i^{\pm}}{\partial t^3}=i\gamma_i\left(\left|A_i^{\pm}\right|^2+2\sum\nolimits_{k\neq i}\left|A_k^{\pm}\right|^2\right)A_i^{\pm}+i\frac{2\pi\omega_i}{c}P_{\omega,i}$$
$$+\frac{g_R(\Delta\omega)}{2}\left(\left|A_{i-1}^{\pm}\right|^2+\left|A_{i-1}^{\mp}\right|^2\right)A_i^{\pm}-\frac{g_R(\Delta\omega)}{2}\left(\left|A_{i+1}^{\pm}\right|^2+\left|A_{i+1}^{\mp}\right|^2\right)A_i^{\pm}-\frac{\alpha}{2}A_i^{\pm}-\frac{\varepsilon(\omega)}{2}A_i^{\pm} \quad (12)$$
$$+\frac{\varepsilon(\omega)}{2}A_i^{\mp},(i=1,2,3)$$

$$\pm\frac{\partial A_4^{\pm}}{\partial z}+\frac{1}{v_{g,4}}\frac{\partial A_4^{\pm}}{\partial t}+\frac{i\beta_{2,4}}{2}\frac{\partial^2 A_4^{\pm}}{\partial t^2}-\frac{\beta_{3,4}}{6}\frac{\partial^3 A_4^{\pm}}{\partial t^3}=i\gamma_4\left(\left|A_4^{\pm}\right|^2+2\sum\nolimits_{k\neq 4}\left|A_k^{\pm}\right|^2\right)A_4^{\pm}+i\frac{2\pi\omega_4}{c}P_{\omega,4}$$
$$+\frac{g_R(\Delta\omega)}{2}\left(\left|A_3^{\pm}\right|^2+\left|A_3^{\mp}\right|^2\right)A_4^{\pm}-\frac{\alpha}{2}A_4^{\pm}-\frac{\varepsilon(\omega)}{2}A_4^{\pm}+\frac{\varepsilon(\omega)}{2}A_4^{\mp} \quad (13)$$

where A is the complex amplitude of the optical field, superscripts + and − represent the forward and backward propagating lights. The subscripts 0 to 4 denote the 1070 nm light, the 1120 nm first-order Stokes wave, the 1178 nm second-order Stokes wave, the 1243 nm third-order Stokes wave, and the 1310 nm fourth-order Stokes wave, respectively. The v_g is the group velocity, the β_2 and β_3 are the second and third-order dispersion coefficient, respectively. γ is the nonlinear parameter. $g_R(\Delta\omega)$ is the Raman gain of different frequency shift, α is the loss coefficient, and $\varepsilon(\omega)$ is the Rayleigh scattering coefficient of different wavelengths. It should be noted that the second term on the right side of Eqs. (4-6) represents the conversion of FW to SH, and this term is equivalent to Eq. (2). Therefore, together with Eqs. (1) and (3), we can simulate the simultaneous evolution of FW and SH in our structure.

The simulated output spectrum of the FW is shown in Fig. 5(a). Several main spectral peaks align with the experimental results. The evolution of the spectrum along the fiber is shown in Fig. 5(b). The energy of the 1070 nm light quickly converts to Raman light.

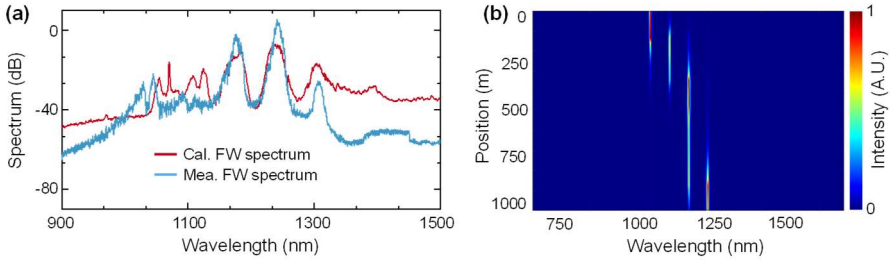

Fig.5. Simulated (a) output spectrum and (b) spectral evolution along the passive fiber of the FW.

The evolution of the SH spectrum and the final output spectrum are shown in Figs. 6(a) and (b). The intensity of the FW is a determining factor for SH gain. FWs that do not rapidly convert to other wavelengths corresponds to stronger SH gain. According to the simulation results, the frequency-doubled light of the first, second, and third-order Stokes wave dominates. However, the simulated pedestal is lower, which is because the pedestal is primarily generated by nonlinear interactions between different wavelengths. In our model, the nonlinear effects within the SH band itself were not considered. Fig. 6(c) shows the SH conversion efficiency for different lengths of GDF, with the highest conversion efficiency occurring around 1000 meters, which is why experiments are conducted at this length.

https://doi.org/10.1017/hpl.2025.25 Published online by Cambridge University Press

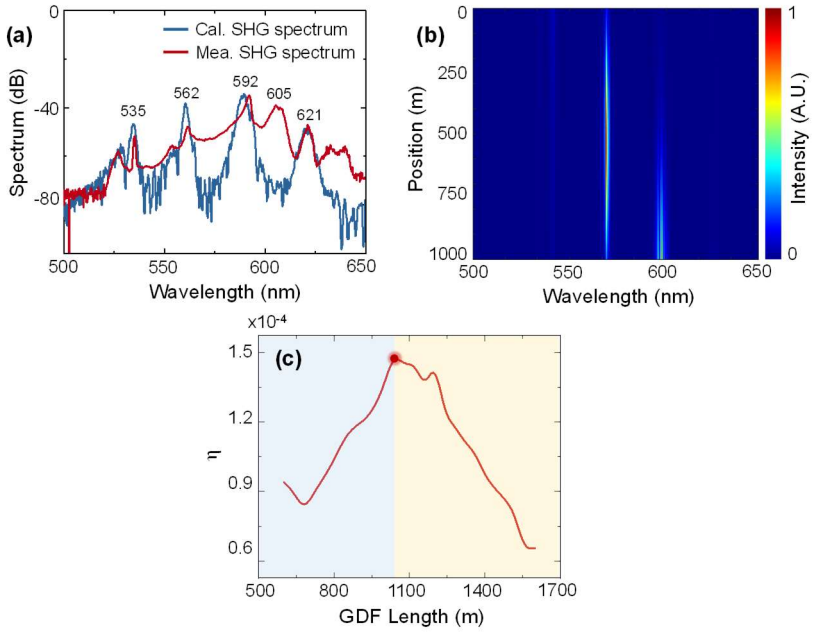

Fig.6. Simulated (a) output spectrum and (b) spectral evolution along the passive fiber of the SH. (c) The SH conversion efficiency with different GDF lengths.

To verify whether the FLM provides feedback to the SH, its internal spectrum is also measured. Employing a 99/1 coupler, a portion of the internal light is extracted and measured. The visible light spectrum indicates that point feedback plays a role, as detailed in Note S5, Supplementary material. Furthermore, simulation analysis shows that the feedback intensity of point feedback can influence the SH power; however, SHG can still occur even when the feedback intensity is weakened. Using a long fiber, we explore another possibility for providing backward light feedback. This is also distributed feedback, where the feedback for visible light is stronger than that for near-infrared light. The laser structure and output spectra are presented in Note S6, Supplementary material. The SH components demonstrate that effective SHG occurs even under weak feedback conditions. Thus, the structure for achieving in-core SHG using an all-fiber RFL can be diverse.

4. Conclusion

In summary, we introduce a broadband-distributed feedback RFL capable of realizing in-core second-order nonlinear process, specifically SHG. The passive spatiotemporal gain modulation of the RFL and the extended fiber enhances the SH gain. The random cavity for the SH is formed by distributed feedback and point feedback. A maximum output power of 10.06 mW for the SH band is realized. Temporal analyses reveal the occurrence of optical rogue waves, with statistical analysis indicating that higher pump power may be able to mitigate their appearance probability. A theoretical model for SHG in the RFL is shown, and further coupled with the GNLSEs to solve the broad-spectrum evolution more accurately. Our research introduces an all-fiber in-core SHG approach that requires no special treatment and exhibits strong pumping injection capability. Moreover, this structure can simultaneously generate FW and SH, offering a highly integrated design. Further studies might include the design of feedback response for SH wavelength tuning, increasing pump power for higher-power applications, in-depth investigation of rogue waves. We believe the simple method we

https://doi.org/10.1017/hpl.2025.25 Published online by Cambridge University Press

demonstrate for generating in-core SH may be able to support further research on in-core second-order nonlinear effects and RFLs.

Acknowledgements

The authors acknowledge the financial support from the National Natural Science Foundation of China (62122040, 62075113).

Disclosures.

The authors declare no conflicts of interest.

Data availability.

Data underlying the results presented in this paper are not publicly available at this time but may be obtained from the authors upon reasonable request.

References

[1] K. Kikuchi, Fundamentals of Coherent Optical Fiber Communications, J. Lightwave Technol. 34 (2016) 157–179. https://doi.org/10.1109/JLT.2015.2463719.
[2] I. Ashry, Y. Mao, B. Wang, F. Hveding, A. Bukhamsin, T.K. Ng, B.S. Ooi, A Review of Distributed Fiber–Optic Sensing in the Oil and Gas Industry, J. Lightwave Technol. 40 (2022) 1407–1431. https://doi.org/10.1109/JLT.2021.3135653.
[3] D. Lo Presti, C. Massaroni, C.S. Jorge Leitao, M. De Fatima Domingues, M. Sypabekova, D. Barrera, I. Floris, L. Massari, C.M. Oddo, S. Sales, I.I. Iordachita, D. Tosi, E. Schena, Fiber Bragg Gratings for Medical Applications and Future Challenges: A Review, IEEE Access 8 (2020) 156863–156888. https://doi.org/10.1109/ACCESS.2020.3019138.
[4] S. Aparanji, M. Zhao, V.J. Srinivasan, Decoding diffuse light scattering dynamics in layered tissues: path length versus fluctuation time scale, Opt. Lett. 48 (2023) 6056. https://doi.org/10.1364/OL.507162.
[5] N. Borhani, E. Kakkava, C. Moser, D. Psaltis, Learning to see through multimode fibers, Optica 5 (2018) 960. https://doi.org/10.1364/OPTICA.5.000960.
[6] M. Zhao, W. Zhou, S. Aparanji, D. Mazumder, V.J. Srinivasan, Interferometric diffusing wave spectroscopy imaging with an electronically variable time-of-flight filter, Optica 10 (2023) 42. https://doi.org/10.1364/OPTICA.472471.
[7] J.M. Fini, M.D. Mermelstein, M.F. Yan, R.T. Bise, A.D. Yablon, P.W. Wisk, M.J. Andrejco, Distributed suppression of stimulated Raman scattering in an Yb-doped filter-fiber amplifier, Opt. Lett. 31 (2006) 2550. https://doi.org/10.1364/OL.31.002550.
[8] Y. Fujii, B.S. Kawasaki, K.O. Hill, D.C. Johnson, Sum-frequency light generation in optical fibers, Opt. Lett. 5 (1980) 48. https://doi.org/10.1364/OL.5.000048.
[9] A. Mocofanescu, L. Wang, R. Jain, K.D. Shaw, A. Gavrielides, P. Peterson, M.P. Sharma, SBS threshold for single mode and multimode GRIN fibers in an all fiber configuration, Opt. Express 13 (2005) 2019. https://doi.org/10.1364/OPEX.13.002019.
[10] G. Rademacher, R.S. Luis, B.J. Puttnam, H. Furukawa, R. Maruyama, K. Aikawa, Y. Awaji, N. Wada, Investigation of Intermodal Four-Wave Mixing for Nonlinear Signal Processing in Few-Mode Fibers, IEEE Photon. Technol. Lett. 30 (2018) 1527–1530. https://doi.org/10.1109/LPT.2018.2856755.
[11] D. Zhao, B. Zhang, X. Zhu, S. Liu, L. Jiang, Z. Dou, L. Yang, J. Hou, 2.1 μm, high-energy dissipative soliton resonance from a holmium-doped fiber laser system, High Pow Laser Sci Eng 11 (2023) e12. https://doi.org/10.1017/hpl.2023.3.
[12] H. Zhang, P. Zhou, H. Xiao, J. Leng, R. Tao, X. Wang, J. Xu, X. Xu, Z. Liu, Toward high-power nonlinear fiber amplifier, High Pow Laser Sci Eng 6 (2018) e51. https://doi.org/10.1017/hpl.2018.45.
[13] H. Wu, P. Wang, J. Song, J. Ye, J. Xu, X. Li, P. Zhou, High power tunable mid-infrared optical parametric oscillator enabled by random fiber laser, Opt. Express 26 (2018) 6446. https://doi.org/10.1364/OE.26.006446.
[14] T. Qi, Y. Yang, D. Li, P. Yan, M. Gong, Q. Xiao, Kilowatt-Level Supercontinuum Generation in Random Raman Fiber Laser Oscillator With Full-Open Cavity, J. Lightwave Technol. 40 (2022) 7159–7166. https://doi.org/10.1109/JLT.2022.3197829.
[15] H. Wu, Z. Wang, Q. He, W. Sun, Y. Rao, Common-cavity ytterbium/Raman random distributed feedback fiber laser, Laser Phys. Lett. 14 (2017) 065101. https://doi.org/10.1088/1612-202X/aa6dbf.
[16] D.R. Solli, C. Ropers, P. Koonath, B. Jalali, Optical rogue waves, Nature 450 (2007) 1054–1057. https://doi.org/10.1038/nature06402.

[17] X. Wei, Z. He, W. Zhang, Cascaded supercontinuum generation and rogue wave harnessing, Chaos, Solitons & Fractals 165 (2022) 112858. https://doi.org/10.1016/j.chaos.2022.112858.
[18] D.L. Nicácio, E.A. Gouveia, N.M. Borges, A.S. Gouveia-Neto, Third-harmonic generation in GeO2-doped silica single-mode optical fibers, Applied Physics Letters 62 (1993) 2179–2181. https://doi.org/10.1063/1.109461.
[19] V. Grubsky, J. Feinberg, Phase-matched third-harmonic UV generation using low-order modes in a glass micro-fiber, Optics Communications 274 (2007) 447–450. https://doi.org/10.1016/j.optcom.2007.02.023.
[20] V. Grubsky, A. Savchenko, Glass micro-fibers for efficient third harmonic generation, Opt. Express 13 (2005) 6798. https://doi.org/10.1364/OPEX.13.006798.
[21] Y. Chen, Y. Zhou, Z. Qin, G. Xie, P. Yuan, J. Ma, L. Qian, Spatiotemporally mode-locked soliton fiber laser at 2.8 μm, High Pow Laser Sci Eng 11 (2023) e59. https://doi.org/10.1017/hpl.2023.58.
[22] J. He, J. Ye, Y. Ke, X. Ma, Y. Zhang, J. Liang, L. Du, W. Chen, J. Zou, J. Xu, J. Leng, P. Zhou, Spectral channels increase of multi-wavelength visible laser enabled by SHG-SFG hybrid processes, (n.d.).
[23] E.I. Dontsova, S.I. Kablukov, I.D. Vatnik, S.A. Babin, Frequency doubling of Raman fiber lasers with random distributed feedback, Opt. Lett. 41 (2016) 1439–1442.
[24] S. Rota-Rodrigo, B. Gouhier, C. Dixneuf, L. Antoni-Micollier, G. Guiraud, D. Leandro, M. Lopez-Amo, N. Traynor, G. Santarelli, Watt-level green random laser at 532 nm by SHG of a Yb-doped fiber laser, Opt. Lett. 43 (2018) 4284. https://doi.org/10.1364/OL.43.004284.
[25] A.S.L. Gomes, U. ÖSterberg, J.R. Taylor, Spectral and temporal investigations of nonlinearities in a non-polarization preserving single-mode optical fibre, Appl. Phys. B 41 (1986) 235–240. https://doi.org/10.1007/BF00697404.
[26] R.H. Stolen, H.W.K. Tom, Self-organized phase-matched harmonic generation in optical fibers, Opt. Lett. 12 (1987) 585. https://doi.org/10.1364/OL.12.000585.
[27] U. Österberg, W. Margulis, Dye laser pumped by Nd:YAG laser pulses frequency doubled in a glass optical fiber, Opt. Lett. 11 (1986) 516. https://doi.org/10.1364/OL.11.000516.
[28] J.M. Gabriagues, H. Février, Analysis of frequency-doubling processes in optical fibers using Raman spectroscopy, Opt. Lett. 12 (1987) 720. https://doi.org/10.1364/OL.12.000720.
[29] R.W. Terhune, D.A. Weinberger, Second-harmonic generation in fibers, J. Opt. Soc. Am. B 4 (1987) 661. https://doi.org/10.1364/JOSAB.4.000661.
[30] K. Chikuma, S. Umegaki, Theory of optical second-harmonic generation in crystal-cored fibers based on phase matching of Čerenkov-type radiation, J. Opt. Soc. Am. B 9 (1992) 1083. https://doi.org/10.1364/JOSAB.9.001083.
[31] B.P. Antonyuk, V.B. Antonyuk, High efficient second harmonic generation in Ge-doped silica fibers, Optics Communications 147 (1998) 143–147. https://doi.org/10.1016/S0030-4018(97)00565-8.
[32] D.Z. Anderson, V. Mizrahi, J.E. Sipe, Model for second-harmonic generation in glass optical fibers based on asymmetric photoelectron emission from defect sites, Opt. Lett. 16 (1991) 796. https://doi.org/10.1364/OL.16.000796.
[33] S. Majchrowska, J. Pabisiak, T. Martynkien, P. Mergo, K. Tarnowski, Influence of attenuation on self-organized second-harmonic generation in a germanium-doped microstructured silica fiber, Opt. Lett. 43 (2018) 2791. https://doi.org/10.1364/OL.43.002791.
[34] G.P. Agrawal, Nonlinear Fiber Optics, Elsevier Science, 2013. https://books.google.co.jp/books?id=xNvw-GDVn84C.
[35] T.E. Tsai, M.A. Saifi, E.J. Friebele, U. Österberg, D.L. Griscom, Correlation of defect centers with second-harmonic generation in Ge-doped and Ge–P-doped silica-core single-mode fibers, Opt. Lett. 14 (1989) 1023. https://doi.org/10.1364/OL.14.001023.
[36] T.J. Driscoll, N.M. Lawandy, A. Killian, L. Rienhart, T.F. Morse, Observation of frequency doubling in tantalum doped silica fibres, Electron. Lett. 27 (1991) 2088. https://doi.org/10.1049/el:19911293.
[37] S. Wang, Z. Chen, N. Chen, W. Xu, Q. Hao, S. Liu, Thermal Poling of New Double-Hole Optical Fibers, Applied Sciences 9 (2019) 2176. https://doi.org/10.3390/app9112176.
[38] A. Canagasabey, C. Corbari, A.V. Gladyshev, F. Liegeois, S. Guillemet, Y. Hernandez, M.V. Yashkov, A. Kosolapov, E.M. Dianov, M. Ibsen, P.G. Kazansky, High-average-power second-harmonic generation from periodically poled silica fibers, Opt. Lett. 34 (2009) 2483. https://doi.org/10.1364/OL.34.002483.
[39] R. Kashyap, Phase-matched second-harmonic generation in periodically poled optical fibers, Applied Physics Letters 58 (1991) 1233–1235. https://doi.org/10.1063/1.104372.
[40] S. Richard, Second-harmonic generation in tapered optical fibers, J. Opt. Soc. Am. B 27 (2010) 1504. https://doi.org/10.1364/JOSAB.27.001504.
[41] G.Q. Ngo, E. Najafidehaghani, Z. Gan, S. Khazaee, M.P. Siems, A. George, E.P. Schartner, S. Nolte, H. Ebendorff-Heidepriem, T. Pertsch, A. Tuniz, M.A. Schmidt, U. Peschel, A. Turchanin, F. Eilenberger, In-fibre second-harmonic generation with embedded two-dimensional materials, Nat. Photon. 16 (2022) 769–776. https://doi.org/10.1038/s41566-022-01067-y.
[42] J.-M. Ménard, P. St.J. Russell, Phase-matched electric-field-induced second-harmonic generation in Xe-filled hollow-core photonic crystal fiber, Opt. Lett. 40 (2015) 3679. https://doi.org/10.1364/OL.40.003679.
[43] Z. Hao, B. Jiang, Y. Ma, R. Yi, X. Gan, J. Zhao, Broadband and continuous wave pumped second-harmonic generation from microfiber coated with layered GaSe crystal, OEA 6 (2023) 230012–230012. https://doi.org/10.29026/oea.2023.230012.

https://doi.org/10.1017/hpl.2025.25 Published online by Cambridge University Press

[44] T. Cheng, W. Gao, H. Kawashima, D. Deng, M. Liao, M. Matsumoto, T. Misumi, T. Suzuki, Y. Ohishi, Widely tunable second-harmonic generation in a chalcogenide–tellurite hybrid optical fiber, Opt. Lett. 39 (2014) 2145. https://doi.org/10.1364/OL.39.002145.

[45] J. Chen, J. Tan, G. Wu, X. Zhang, F. Xu, Y. Lu, Tunable and enhanced light emission in hybrid WS2-optical-fiber-nanowire structures, Light Sci Appl 8 (2019) 8. https://doi.org/10.1038/s41377-018-0115-9.

[46] B. Jiang, Z. Hao, Y. Ji, Y. Hou, R. Yi, D. Mao, X. Gan, J. Zhao, High-efficiency second-order nonlinear processes in an optical microfibre assisted by few-layer GaSe, Light Sci Appl 9 (2020) 63. https://doi.org/10.1038/s41377-020-0304-1.

[47] S. Aparanji, V. Balaswamy, S. Arun, V.R. Supradeepa, Observation of a rainbow of visible colors in a near infrared cascaded Raman fiber laser and its novel application as a diagnostic tool for length resolved spectral analysis, in: K.L. Vodopyanov, K.L. Schepler (Eds.), Nonlinear Frequency Generation and Conversion: Materials and Devices XVII, SPIE, San Francisco, United States, 2018: p. 21. https://doi.org/10.1117/12.2289817.

[48] S. Aparanji, S. Arun, V. Balaswamy, V.R. Supradeepa, Visible light generation in the cladding of optical fibers carrying near-infrared continuous-wave lasers due to Cherenkov-phase matched harmonic conversion, Opt. Lett. 45 (2020) 993. https://doi.org/10.1364/OL.384581.

[49] S. Lin, Z. Wang, J. Li, S. Chen, Y. Rao, G. Peng, A.S.L. Gomes, Nonlinear dynamics of four-wave mixing, cascaded stimulated Raman scattering and self Q-switching in a common-cavity ytterbium/Raman random fiber laser, Optics & Laser Technology 134 (2021) 106613. https://doi.org/10.1016/j.optlastec.2020.106613.

[50] J. He, R. Song, L. Jiang, W. Yang, J. Hou, Supercontinuum generated in an all-polarization-maintaining random fiber laser structure, Opt. Express 29 (2021) 28843. https://doi.org/10.1364/OE.434691.

[51] S. Perret, G. Fanjoux, L. Bigot, J. Fatome, G. Millot, J.M. Dudley, T. Sylvestre, Supercontinuum generation by intermodal four-wave mixing in a step-index few-mode fibre, APL Photonics 4 (2019) 022905. https://doi.org/10.1063/1.5045645.

[52] L. Chen, R. Song, C. Lei, W. Yang, J. Hou, Random fiber laser directly generates visible to near-infrared supercontinuum, Opt. Express 27 (2019) 29781. https://doi.org/10.1364/OE.27.029781.

[53] L. Jiang, R. Song, J. Hou, Hundred-watt level all-fiber visible supercontinuum generation from a graded-index multimode fiber, Chin. Opt. Lett. 21 (2023) 051403. https://doi.org/10.3788/COL202321.051403.

[54] G. Lopez-Galmiche, Z. Sanjabi Eznaveh, M.A. Eftekhar, J. Antonio Lopez, L.G. Wright, F. Wise, D. Christodoulides, R. Amezcua Correa, Visible supercontinuum generation in a graded index multimode fiber pumped at 1064 nm, Opt. Lett. 41 (2016) 2553. https://doi.org/10.1364/OL.41.002553.

[55] L.G. Wright, S. Wabnitz, D.N. Christodoulides, F.W. Wise, Ultrabroadband Dispersive Radiation by Spatiotemporal Oscillation of Multimode Waves, Phys. Rev. Lett. 115 (2015) 223902. https://doi.org/10.1103/PhysRevLett.115.223902.

[56] K. Krupa, A. Tonello, A. Barthélémy, V. Couderc, B.M. Shalaby, A. Bendahmane, G. Millot, S. Wabnitz, Observation of Geometric Parametric Instability Induced by the Periodic Spatial Self-Imaging of Multimode Waves, PHYSICAL REVIEW LETTERS (2016).

[57] D. Ceoldo, K. Krupa, A. Tonello, V. Couderc, D. Modotto, U. Minoni, G. Millot, S. Wabnitz, Second harmonic generation in multimode graded-index fibers: spatial beam cleaning and multiple harmonic sideband generation, Opt. Lett. 42 (2017) 971. https://doi.org/10.1364/OL.42.000971.

[58] I.D. Vatnik, D.V. Churkin, E.V. Podivilov, S.A. Babin, High-efficiency generation in a short random fiber laser, Laser Phys. Lett. 11 (2014) 075101. https://doi.org/10.1088/1612-2011/11/7/075101.

[59] V. Balaswamy, S. Aparanji, S. Arun, S. Ramachandran, V.R. Supradeepa, High-power, widely wavelength tunable, grating-free Raman fiber laser based on filtered feedback, Opt. Lett. 44 (2019) 279. https://doi.org/10.1364/OL.44.000279.

[60] V. Balaswamy, S. Arun, S. Aparanji, V. Choudhury, V.R. Supradeepa, High-power, fixed, and tunable wavelength, grating-free cascaded Raman fiber lasers, Opt. Lett. 43 (2018) 1574. https://doi.org/10.1364/OL.43.001574.

[61] S. Aparanji, V. Balaswamy, S. Arun, V.R. Supradeepa, Simultaneous Raman based power combining and wavelength conversion of high-power fiber lasers, Opt. Express 26 (2018) 4954. https://doi.org/10.1364/OE.26.004954.

[62] J. Xu, J. Ye, W. Liu, J. Wu, H. Zhang, J. Leng, P. Zhou, Passively spatiotemporal gain-modulation-induced stable pulsing operation of a random fiber laser, Photon. Res. 5 (2017) 598. https://doi.org/10.1364/PRJ.5.000598.

[63] S.K. Turitsyn, S.A. Babin, A.E. El-Taher, P. Harper, D.V. Churkin, S.I. Kablukov, J.D. Ania-Castañón, V. Karalekas, E.V. Podivilov, Random distributed feedback fibre laser, Nature Photon 4 (2010) 231–235. https://doi.org/10.1038/nphoton.2010.4.

[64] A.A. Fotiadi, P. Mégret, M. Blondel, Dynamics of a self-Q-switched fiber laser with a Rayleigh–stimulated Brillouin scattering ring mirror, Opt. Lett. 29 (2004) 1078. https://doi.org/10.1364/OL.29.001078.

[65] B. Velpula, R. Prakash, V. Choudhury, S. Aparanji, B.S. Vikram, V.R. Supradeepa, Experimental analysis of stimulated Brillouin enhancement in high power, line-broadened, narrow-linewidth fiber amplifiers due to spectral overlap between the Brillouin gain spectrum and the signal back-scatter from the fiber termination, in: P.G. Schunemann, K.L. Schepler (Eds.), Nonlinear Frequency Generation and Conversion: Materials and Devices XVIII, SPIE, San Francisco, United States, 2019: p. 51. https://doi.org/10.1117/12.2510317.

[66] V. Choudhury, S. Aparanji, R. Prakash, V. Balaswamy, V.R. Supradeepa, Visible light flashes induced by pulsed stimulated Brillouin scattering in narrow-linewidth, high-power, near-IR fiber lasers, J. Opt. 23 (2021) 075501. https://doi.org/10.1088/2040-8986/ac0007.
[67] J.M. Dudley, F. Dias, M. Erkintalo, G. Genty, Instabilities, breathers and rogue waves in optics, Nature Photon 8 (2014) 755–764. https://doi.org/10.1038/nphoton.2014.220.
[68] B.P. Antonyuk, Light-driven alignment, Springer, Berlin, 2009.

https://doi.org/10.1017/hpl.2025.25 Published online by Cambridge University Press